第 41 卷 第 12 期
2020 年 12 月
焊 接 学 报
TRANSACTIONS OF THE CHINA WELDING INSTITUTION
Vol. 41(12):80 − 85
December 2020

冲击能量对Fe-C-Mo-V堆焊合金抗磨粒磨损性能的影响

黄智泉， 段嘉旭， 杨威， 张海燕
(郑州机械研究所有限公司, 郑州, 450001)

摘要: 采用含 Fe-C-Mo-V 的气体保护药芯焊丝堆焊制备磨损试样, 并对其进行不同冲击能量下的动载冲击磨粒磨损试验. 通过扫描电子显微镜配合能谱分析、磨损失重测试和激光扫描共聚焦显微镜观察等测试方法, 对熔敷金属的显微组织及磨痕特征进行分析及表征, 研究了熔敷金属在不同冲击能量下的磨粒磨损行为. 结果表明, 熔敷金属的显微组织主要由奥氏体基体、层片状共晶组织及团块状的 VC 硬质相构成. 熔敷金属的磨损失重、磨痕粗糙度以及磨痕深度均随冲击能量的增加而逐渐减小. 磨损机制为磨粒对奥氏体基体的微观切削以及塑性变形. 随着冲击能量的增加, 熔敷金属产生加工硬化, 磨痕亚表面出现形变马氏体组织, 且 VC 硬质相与层片状共晶组织相互作用, 共同提高堆焊层的硬度, 从而提高基体的耐磨性, 增强抗冲击性能.

关键词: Fe-C-Mo-V 堆焊合金; 冲击能量; 磨粒磨损; 形变马氏体
中图分类号: TG 455　　**文献标识码:** A　　**doi:** 10. 12073/j. hjxb. 20200228001

0 序言

随着工业的不断发展, 工具在使用过程中难以避免发生磨损, 在交变载荷下长期运行也会使工件亚表层萌生裂纹. 例如振动筛、耐磨板、破碎机、平地机刮板等地面接合工具, 都是在严重磨损的工况下应用的工具[1]. 应用堆焊修复工艺, 有效恢复零部件的尺寸并使得零部件表面获得良好的耐腐蚀、耐磨、耐高温等性能, 显著提高服役寿命[2-3]. 近年来, 通过向 Fe-C-Mo 系堆焊合金加入钒 (V) 元素生成硬度高的团球状 VC, 提高材料阻挡磨粒的显微切削作用, 在复杂的冲击工况下满足较好的耐磨性[4-5]. 目前 Fe-C-Mo-V 合金系耐磨性的研究主要集中在合金成分调控, 缺乏在特定磨损条件下耐磨性能的研究[6-7].

利用熔化极气体保护焊技术 (GMAW) 制备 Fe-C-Mo-V 堆焊合金, 采用基于 GB/T 2611—1992 规范下的动载冲击三体磨粒磨损系统, 在不同法向冲击能量 (1 ~ 7 J) 条件下, 进行 Fe-C-Mo-V 堆焊合金的动载冲击磨损试验, 研究 Fe-C-Mo-V 堆焊合金在动载冲击环境下的三体磨粒磨损行为.

1 试验材料及方法

1.1 试样制备

焊丝选用郑州机械研究所有限公司自制的 Fe-C-Mo-V 气体保护药芯焊丝, 直径 ϕ1. 6 mm, 堆焊母材为 Q235 钢板, 尺寸为 220 mm × 160 mm × 25 mm. 堆焊前将母材表面用砂轮打磨出金属光泽, 采用熔化极气体保护焊制备熔敷金属, 保护气体为 95% Ar + 5% CO_2. 焊接工艺参数如表 1 所示, 在焊接过程中, 采用连续焊三层, 每层五道, 搭接量为 1/3 ~ 1/4, 焊前不预热, 焊后用玻璃棉包裹缓冷. 堆焊完成后进行熔覆金属的化学成分检测, 结果如表 2 所示.

表 1 焊接工艺参数
Table 1 Welding parameter of hardfacing alloys

焊接电压 U/V	焊接电流 I/A	焊枪行进速度 v_1/(mm·s^{-1})	气体流量 q/(L·min^{-1})	单道焊缝宽度 H_1/mm	焊缝总厚度S/mm
30 ~ 32	280 ~ 320	3. 3 ~ 4. 5	15 ~ 17	25 ~ 30	8 ~ 12

1.2 试验方法

采用 MLD-10 型的动载冲击三体磨损试验机

收稿日期: 2020 − 02 − 28
基金项目: 郑州市重大科技创新专项资助项目 (188PCXZX784)

表 2　熔敷金属主要化学成分 (质量分数，%)

Table 2　Chemical composition of deposited metals

C	Si	Mn	Ni	Mo	V	Fe
1.0 ~ 2.5	1.5 ~ 2.0	1.72 ~ 2.0	0.1 ~ 0.5	15.0 ~ 20.0	5.0 ~ 10.0	余量

进行磨粒磨损试验，磨损试验参数如表 3 所示，磨粒采用铸造石英砂. 试验过程中冲锤可上移至固定的最大高度后自由落体，使方形上试样冲击旋转的环形下试样，造成冲击磨损，同时在冲锤被提升之前还要发生一段时间的滑动磨损. 冲击能量 A_k(J) 是通过计算冲锤重量 P(N) 与冲锤自由落体高度 H(mm) 的乘积得到. 冲锤重量为 100 N 时，适用于 1 ~ 5 J 冲击能量，冲锤重量为 160 N 时，适用于 6 ~ 7 J 冲击能量. 试验所需磨损试样用电火花切割技术在堆焊试板上切取规格为 30 mm × 10 mm × 10 mm 的方形试样，表面粗糙度 R_a < 1.6 μm. 下试样为购置的具有良好耐磨性能，受冲击变形量小的 NM450 钢板，加工成外径 ϕ50 mm，内径 ϕ30 mm 的圆环，一个上试样对应一个下试样. 调整冲锤下落高度实现冲击能量 1 ~ 7 J 的变化，磨损试验前后，使用 AL204 型分析天平计算熔敷金属的磨损失重，精确至 0.000 1 g，每个冲击能量下重复 5 次试验，计算失重的平均值.

表 3　磨损试验参数

Table 3　Parameters of abrasive wear test

磨粒直径D/μm	磨粒流速v_2/(g·min^{-1})	冲锤重量P/N	冲锤下落高度H_2/mm	冲击次数T(次)	下试样轴转速n/(r·min^{-1})	冲击能量A_k/J
460 ~ 540	186 ~ 213	100/160	0 ~ 50	6 000	200	1 ~ 7

熔敷金属的物相组成使用 Uitima IV 型 X 射线衍射仪进行检测，参数：Cu-K_α 靶，扫描速度 5°/min，扫描范围 30° ~ 100°. 熔敷金属的显微组织、磨痕微观形貌及磨痕亚表面形貌使用 Phenom Pro XL 型台式扫描电子显微镜进行观察与分析，使用 OLYMPUS LEXT OLS4100 型激光共聚焦显微镜配合 LEXT 分析软件测量磨痕深度 (磨损最充分的面与原始表面高度差) 以及磨痕面粗糙度. 在未磨损的熔敷金属的预磨面及磨损后的磨痕表面通过 Wolpert 401 MVD 数显维氏硬度计进行硬度检测，控制载荷 1.96 N，保荷 15 s.

2　试验结果及分析

2.1　熔敷金属显微组织及硬度分析

图 1 为 Fe-C-Mo-V 堆焊合金的 X 射线衍射分析结果，可检测到的物相有 γ-Fe，α-Fe，马氏体，VC，M_2C (M = Fe, Mo) 以及 M_3C (M = Fe, Mo) 型碳化物. 图 2 为熔敷金属光学显微镜下的金相组织形貌. 由图 2 可知，熔敷金属的显微组织主要由三部分构成，奥氏体基体、密集分布在基体上的层片状共晶组织，以及在层片状组织和基体上弥散分布的团块状 VC (2 615.43 HV0.2) 硬质相. 其中基体中存在合金元素的固溶强化，硬度可达 885.5 HV0.2，层片状共晶组织主要为 M_3C (M = Fe, Mo)，Mo_2C 等的复合物，硬度可达 1 240.31 HV0.2.

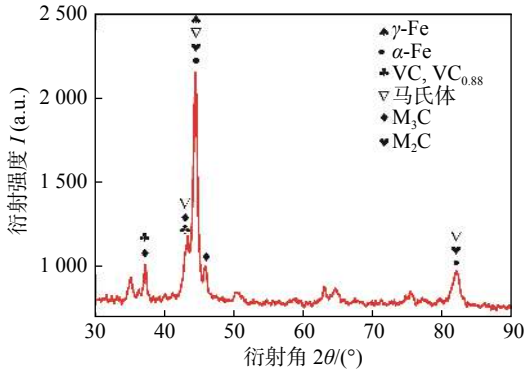

图 1　熔敷金属 XRD 分析

Fig. 1　X-ray diffraction patterns of deposited metals

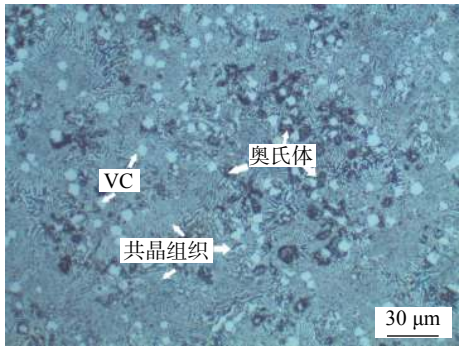

图 2　熔敷金属 OM 分析

Fig. 2　OM image of deposited metals

试验测得堆焊合金熔敷金属的显微硬度为840 ~ 920 HV0.2, 尽管密集分布的高硬度团块状VC以及层片状复合碳化物能对基体形成保护, 不易产生应力集中, 在石英砂冲击磨损环境下能较好抵抗磨粒的侵蚀[8], 但奥氏体基体的硬度仍低于石英砂的硬度 1 000 ~ 1 200 HV0.2, 能够造成充分磨损[9].

2.2 熔敷金属磨损损失结果

不同冲击能量条件下熔敷金属磨损后试样的宏观形貌如图 3 所示. 由图 3 可以看到, 当冲击能量较小 (1 ~ 3 J) 时, 宏观磨痕整体上呈较明显的圆弧凹形. 当冲击能量较大 (4 ~ 7 J) 时, 宏观磨痕较为平坦, 几乎观察不到圆弧凹形.

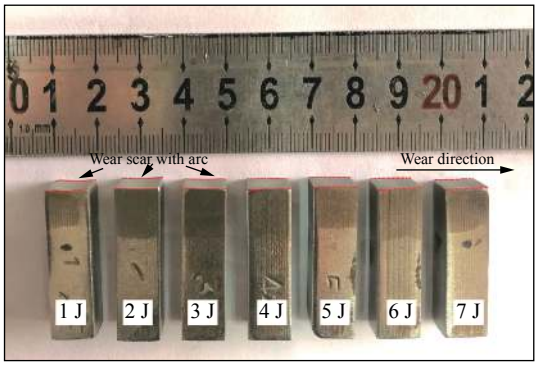

图 3 熔敷金属磨损后试样宏观外形变化

Fig. 3 Macro variation trend of wear scar of deposited metals

不同冲击能量条件下熔敷金属磨损损失检测结果如图 4 所示. 由图 4a 可以看到, 随冲击能量不断增大, 熔敷金属磨损失重先显著减小, 然后趋于保持较低的水平. 根据磨痕深度测试结果 (图 4b), 可以看到, 随冲击能量不断增大, 熔敷金属磨痕深度不断下降, 说明磨损量减少, 磨痕表面平坦. 再结合图 4c 磨痕表面的粗糙度测量可以看出, 随着冲击能量增大, 磨痕微观面粗糙度逐渐下降, 说明磨损无法进一步剧烈进行.

根据能量守恒, 在冲击过程中能量存在快速转换, 冲击动能可以转变为塑性变形消耗的能量、弹性波动消耗的能量、磨粒破碎所能消耗的能量、摩擦产生的热能以及声能等[10]. 当冲击能量较小 (1 ~ 3 J) 时, 方形上试样沿着圆形下环形试样均匀磨损, 接触区域的应力主要是圆形下试样最高点与上块状试样之间的压应力, 并随着冲击过程的深入, 压应力值迅速上升, 最终在试样接触表面形成冲击凹坑[8]. 当冲击能量较大 (4 ~ 7 J) 时, 由于磨粒破碎并

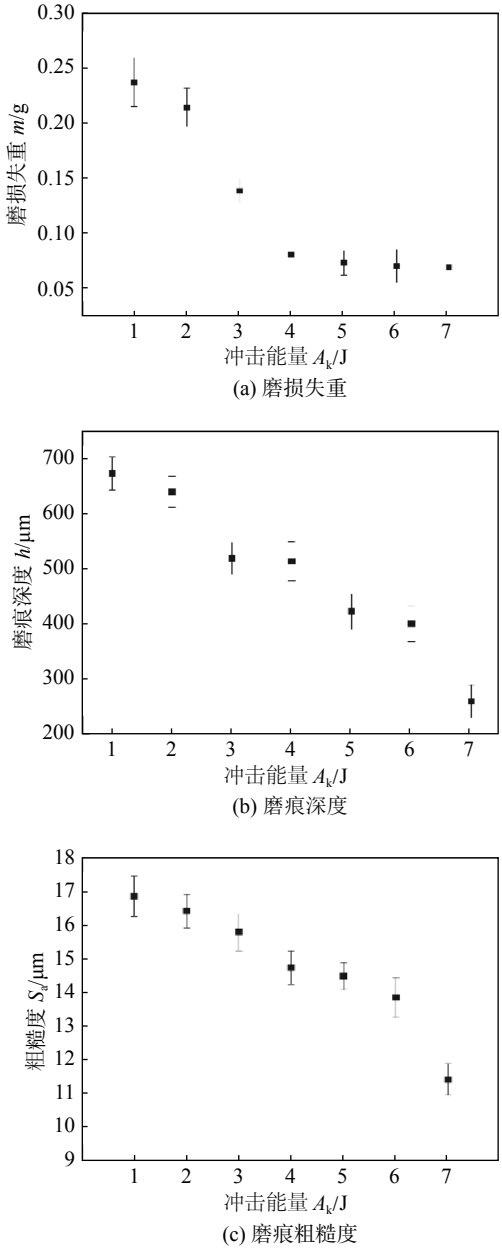

图 4 熔敷金属在不同冲击能量下的磨损变化情况

Fig. 4 Variation trend of wear scar in various normal impact energy of deposited metals. (a) wear loss; (b) wear scar depth; (c) wear roughness

散乱分布在上下试样之间, 导致在滑动磨损时上下试样接触面积增大, 且在反复磨损过程中, 磨粒一直把材料推向两边又不断把堆积的材料压平, 最终在试样磨损接触表面出现较为平坦的磨损面[9-11]. 因此可以认为, 随冲击能量不断增大, 堆焊合金的磨损程度逐渐减小, 磨粒对合金均匀磨损逐渐减弱.

2.3 磨痕微观形貌检测

取 1 和 7 J 两个典型冲击能量条件下熔敷金属磨痕形貌的微观变化 SEM 分析结果, 如图 5 所示, 其中, 图中局部放大如图中右上角所示. 可以看到,

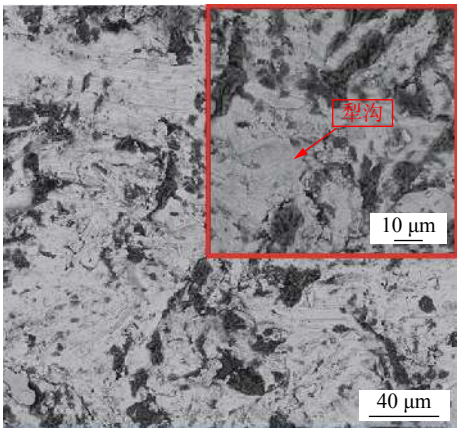

(a) 1 J

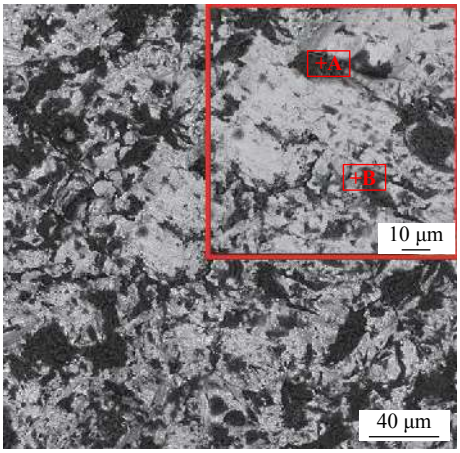

(b) 7 J

图 5　不同冲击能量下熔敷金属的磨痕的 SEM 形貌

Fig. 5　SEM images of wear scars in various normal impact energy of deposited metals.(a) 1 J; (b) 7 J

在低倍下的熔敷金属磨痕上具有显著的黑色区域，随冲击能量增大，黑色区域面积提高.

图 5a 中的局部放大可以看到，当冲击能量较低 (1 J) 时，基体组织上即发生较大幅度的塑性变形，磨痕存在大量长而宽的犁沟，犁沟方向复杂，这是由于磨粒受挤压存在流动的不均匀性. 通过图 6 所示的 EDS 分析结果可以看到黑色区域有夹杂的石英砂以及破碎的 VC 硬质相，白色区域主要为基体组织及网状复合碳化物，存在大量塑性变形，引起材料流动形成犁沟. 根据图 5b 中的局部放大可以看到，当冲击能量较高 (7 J) 时，黑色区域面积增加. 对图 5b 放大图中点 A, B 进行 EDS 分析，结果如图 7 所示，点 A 处黑色区域主要为含 Al 杂质的 SiO_2 石英砂磨粒，点 B 处的剥落坑不仅存在石英砂磨粒，还存在破碎的 VC 硬质相.

在垂直于试样表面的正应力作用下，基体组织发生磨损，导致 VC 硬质相发生破碎和断裂导致脱落，切向滑动分应力对奥氏体基体组织进行切削，形成犁沟[12]. 随冲击能量增大，磨粒挤压进入剥落坑的作用增强，粘附严重且密集，粘附磨粒的形态由条状转变为大片团絮状，磨粒填充局部磨损位置，减小磨痕粗糙度，同时网状结构碳化物可以钉扎基体及碳化钒的剥落，有利于减弱进一步磨损[13-14].

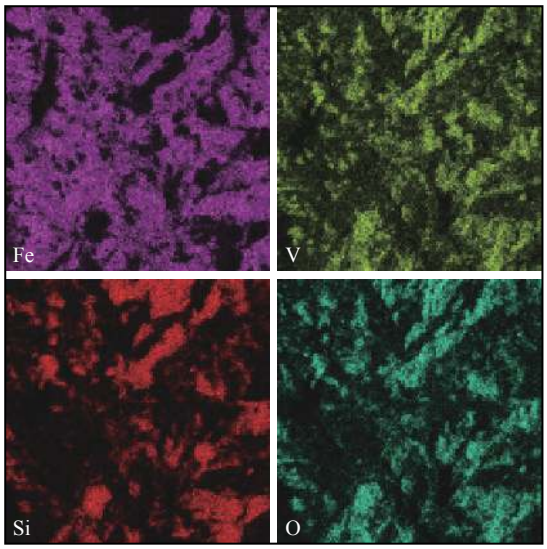

图 6　图 5a 局部放大 EDS 面扫描

Fig. 6　EDS area scan images of enlarge images of Fig.5a

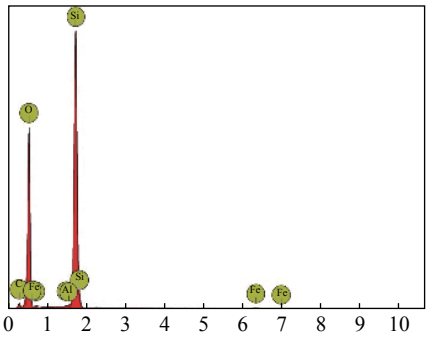

(a) A点扫描图

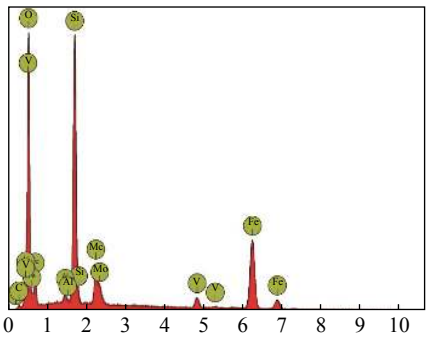

(b) B点扫描图

图 7　图 5b 的 EDS 点扫描图

Fig. 7　EDS spot scan images of in Fig.5b. (a) spot A; (b) spot B

2.4 磨痕硬度及磨痕亚表面形貌变化

对磨痕表面进行维氏硬度的测量，结果如图 8 所示，可以看到，磨损后不同冲击能量下的磨痕表面的硬度皆高于磨损前材料表面的硬度. 冲击磨粒磨损为高应力磨损，金属表面随着磨损的进行表面层会发生如加工硬化、表面晶粒细化等一系列的物理和力学性质的变化以及组织变化，使得基体材料的硬度有大幅度的提高[14-15].

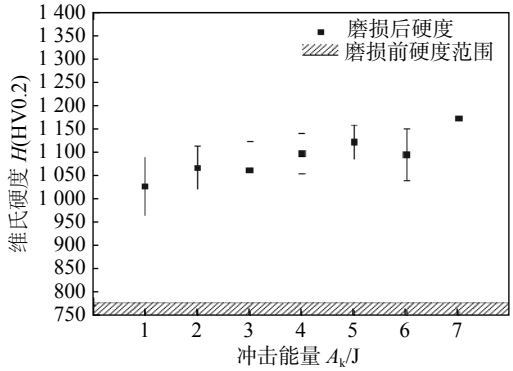

图 8 熔敷金属磨痕硬度

Fig. 8 Wear hardness of deposited metals

取磨损后的试样进行 X 射线衍射分析，进行磨损前后 XRD 分析结果对比，结果如图 9 所示，可以看到奥氏体基体经冲击磨损后转变为马氏体组织，从而提高了熔敷金属的硬度.

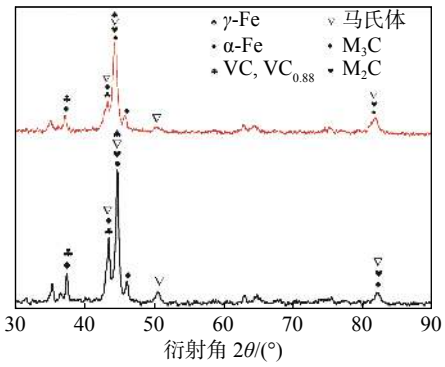

图 9 熔敷金属磨损前后 XRD 分析

Fig. 9 X-ray diffraction patterns of pre-wear and wear scar of deposited metals

取 1 和 7 J 两个典型冲击能量条件下磨痕亚表面形貌 SEM 分析结果，如图 10 所示，可以看到，磨痕亚表面最顶端组织存在方向性，晶粒细化并且存在塑性变形，产生明显的加工硬化现象，出现形变马氏体组织，使得基体的硬度提高. 细小弥散分布的团块状 VC，能够抵抗高应力的作用，再与层片状共晶组织协同作用，使得熔敷金属抵抗磨粒侵蚀的强度提高，因此宏观上表现出磨损失重随冲击能量增加而略微下降的现象.

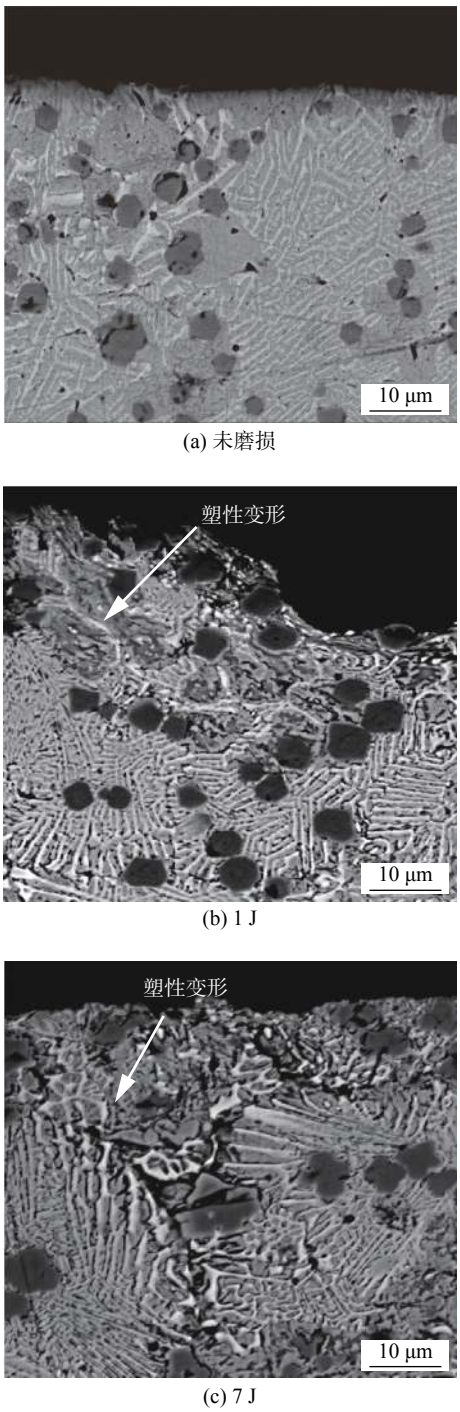

图 10 熔敷金属磨痕亚表面形貌

Fig. 10 Wear scar of subsurface structure of deposited metals. (a) unworn; (b) 1 J; (c) 7 J

3 结论

(1) Fe-C-Mo-V 堆焊合金熔敷金属的显微组织主要由奥氏体基体，层片状共晶组织 (M_3C 和 Mo_2C 复合物) 以及团块状的 VC 硬质相构成，熔敷金属显微硬度为 840 ~ 920 HV0.2.

(2) 随冲击能量增加，磨损失重，磨痕粗糙度，

磨痕深度均减小. 滚动接触导致在小的冲击能量范围内，磨痕具有弧形轮廓，而在高冲击能量范围内，由于磨痕硬化显著，磨损减弱，磨痕较为平整.

(3) Fe-C-Mo-V 堆焊合金熔敷金属在受冲击磨损条件下产生加工硬化现象，奥氏体转变成马氏体组织，提高了基体硬度，团块状 VC 与层片状共晶组织协同保护，使得熔敷金属耐磨性提高，最终导致熔敷金属的磨损失重随冲击能量的增加而减小.

参考文献

[1] 蒋旻, 栗卓新, 王英杰, 等. 含钒耐磨堆焊合金的组织与性能 [J]. 中国机械工程, 2008(13): 1621 − 1625.
Jiang Min, Li Zhuoxin, Wang Yingjie, *et al*. Microstructure and properties of hardfacing alloy containing vanadium[J]. China Mechanical Engineering, 2008(13): 1621 − 1625.

[2] KenchiReddy K M, Jayadeva C T. The effect of microstructure on 3 body abrasive wear behavior of hardfacing alloys[J]. Bonfring International Journal of Industrial Engineering and Management Science, 2014, 4(1): 14 − 23.

[3] 员霄, 王井, 朱青海, 等. H13 钢的铁基和钴基熔覆层组织与耐磨性 [J]. 焊接学报, 2018, 39(12): 105 − 109.
Yun Xiao, Wang Jing, Zhu Qinghai, *et al*. Microstructure and abrasion resistance of Fe-based and Co-based coatings of AISI H13[J]. Transactions of the China Welding Institution, 2018, 39(12): 105 − 109.

[4] Hou T P, Li Y, Wu K M. Effect of high magnetic field on alloy carbide precipitation in an Fe–C–Mo alloy[J]. Journal of Alloys and Compounds, 2012, 527: 240 − 246.

[5] 韩明儒, 魏世忠, 韩华, 等. 新型高钒耐磨合金的组织性能与工程应用 [J]. 热加工工艺, 2015, 44(24): 13 − 15.
Han Mingru, Wei Shizhong, Han Hua, *et al*. Microstructure and properties of new type high vanadium wear-resisting alloy and its engineering application[J]. Hot Working Technology, 2015, 44(24): 13 − 15.

[6] Wieczerzak K, Bala P, Stepien M, *et al*. Formation of eutectic carbides in Fe–Cr–Mo–C alloy during non-equilibrium crystallization[J]. Materials and Design, 2016, 94: 61 − 68.

[7] Deng Xinke, Zhang Guojun, Wang Tao, *et al*. Investigations on microstructure and wear resistance of Fe-Mo alloy coating fabricated by plasma transferred arc cladding[J]. Surface & Coatings Technology, 2018, 350: 480 − 487.

[8] 吴凯. 冲击功对湿磨衬板用钢在腐蚀条件下冲击磨损性能与机理影响的研究 [D]. 合肥: 合肥工业大学, 2006.
Wu Kai. Research on the effect of impact energy to the impact abrasion properties and mechanisms of the wet mill liner materials used in the corrosive condition[D]. Hefei: Hefei University of Technology, 2006.

[9] 王智慧, 贺定勇, 蒋建敏, 等. Fe-Cr-C 耐磨堆焊合金磨粒磨损行为 [J]. 焊接学报, 2010, 31(11): 73 − 76.
Wang Zhihui, He Dingyong, Jiang Jianmin, *et al*. Abrasive wear behavior of Fe-Cr-C hardfacing alloy[J]. Transactions of the China Welding Institution, 2010, 31(11): 73 − 76.

[10] 王猷. 冲击磨料磨损机理研究 [D]. 昆明: 昆明理工大学, 2003.
Wang You. Mechanism researcch of abrasive wear under impacting condition[D]. Kunming: Kunming University of Science and Technology, 2003.

[11] 王智慧, 贺定勇, 俞长丽, 等. 钒对 Fe-Cr-C 耐磨堆焊层性能的影响 [J]. 焊接学报, 2010, 31(9): 61 − 64.
Wang Zhihui, He Dingyong, Yu Changli, *et al*. Effect of vanadium on property of Fe-Cr-C hardfacing alloy[J]. Transactions of the China Welding Institution, 2010, 31(9): 61 − 64.

[12] 吴松波, 蔡振兵, 林禹, 等. 硬质沙粒对 TC_4 钛合金冲击磨损的损伤行为的研究 [J]. 摩擦学学报, 2018, 38(4): 383 − 390.
Wu Songbo, Cai Zhenbing, Lin Yu, *et al*. Effect of hard sand on the impact wear behavior of TC_4 alloy[J]. Tribology, 2018, 38(4): 383 − 390.

[13] 魏炜, 黄智泉, 张海燕, 等. 钒对铁基碳化钨耐磨堆焊层组织和性能的影响 [J]. 焊接学报, 2019, 40(6): 131 − 136.
Wei Wei, Huang Zhiquan, Zhang Haiyan, *et al*. Effect of vanadium on microstructure and performance of tungsten carbide hardfacing alloys[J]. Transactions of the China Welding Institution, 2019, 40(6): 131 − 136.

[14] 朱志明, 范开果, 刘晗, 等. 残余应力对钢轨焊接接头落锤试验性能的影响 [J]. 焊接学报, 2017, 38(4): 55 − 58.
Zhu Zhiming, Fan Kaiguo, Liu Han, *et al*. Influence of residual stress on drop-weight test performance of rail welded joint[J]. Transactions of the China Welding Institution, 2017, 38(4): 55 − 58.

[15] 黄智泉, 张永生, 禹润缜, 等. 载荷对 Fe–Cr–C–Nb 堆焊合金松散磨粒磨损行为的影响 [J]. 粉末冶金技术, 2019, 37(1): 23 − 29.
Huang Zhiquan, Zhang Yongsheng, Yu Runzhen, *et al*. Effects of load on loosing abrasive wear behavior of Fe–Cr–C–Nb hardfacing alloys[J]. Powder Metallurgy Technology, 2019, 37(1): 23 − 29.

第一作者简介：黄智泉，1969 年出生，硕士，研究员；主要从事耐磨堆焊材料与工艺研究；发表论文 60 余篇；Email：1210362687@qq.com.

（编辑：　郑红）

trostatic attraction; bonding strength

Numerical simulation of flange welding deformation based on dynamic constraint WANG Chenxi, TANG Wencheng (State Key Laboratory of Advanced Manufacturing, Southeast University, Nanjing 211189, China). pp 67-73

Abstract: External constraint has a great influence on welding deformation and is one of the important factors affected on welding deformation. Compared with the traditional rigid constraint, dynamic constraint can reflect the effect of external constraint force in the welding process in real time. In the case of multi-layer and multi-pass cross welding of two welds, a multi-body coupling analysis model was established, and the dynamic constraint force effect caused by the deformation of the low-stiffness fixture due to the deformation of the welds was simulated by using the spring element and considering the feedback of the deformation to the constraint force. The deformation of welded parts were discussed from four factors: constraint stiffness, constraint distance, initial constraint force and constraint width. The results showed that the amount of deformation reduced at different degrees with the values of four restraint variable increasing. The influence trends of the constraint stiffness, the initial constraint force and the constraint width were similar, and the initial constraint force was the most important influence factor. The influence of the restraint distance was minimal and its trend was linear.

Key words: welding deformation; multi-layer and multi-pass welding; dynamic constraints; regression analysis

Effect of LaNd on the spreadability of Ti-13Zr-21Cu-9Ni brazing fillers and the properties of TC4 joint LI Chaojun, YAN Yanfu, REN Xiaofei, WANG Yaming, WANG Hongna (Henan University of Science and Technology, Henan, 471023, China). pp 74-79

Abstract: In order to optimize the properties of Ti-13Zr-21Cu-9Ni brazing fillers and obtain a good performance Ti alloy joint, rare earth element LaNd was added to Ti-13Zr-21Cu-9Ni brazing fillers. The commonly used TC4 alloy was used as the mother The effect of rare earth element LaNd on the spreading performance of Ti-13Zr-21Cu-9Ni brazing fillers and the performance of TC4 joints was studied by vacuum furnace, field emission scanning electron microscope, X-ray diffractometer and other equipment. The results showed that the spread area of Ti-13Zr-21Cu-9Ni-*x*LaNd brazing fillers and the shear strength of Ti-13Zr-21Cu-9Ni-xLaNd/TC4 brazed joints first increased and then decreased with the addition of LaNd increased. When the LaNd addition is 0.3%, Ti-13Zr-21Cu-9Ni-*x*LaNd brazing fillers has the largest spreading area, the maximum value is 0.74 cm^2, which is 88.8% higher than the matrix; when the addition of LaNd continues to increase, the formed Cu_5La phase greatly reduce the spreading performance of the brazing fillers. Ti-13Zr-21Cu-9Ni-*x*LaNd/TC4 brazed joint shear strength reaches the maximum when the LaNd addition is 0.3%, which is 157.1 MPa, which is 45.2% higher than the matrix. Therefore, the optimal addition of LaNd It should be around 0.3%.

Key words: rare earth lanthanum and neodymium; titanium alloy joint; spreadability; shear strength

Study of impact energy on abrasive wear resistance of Fe-C-Mo-V hardfacing alloys HUANG Zhiquan, DUAN Jiaxu, YANG Wei, ZHANG Haiyan (Zhengzhou Research Institute of Mechanical Engineering Co., Ltd., Zhengzhou, 450001,China). pp 80-85

Abstract: Wear samples were prepared by hardfacing welding with Fe-C-Mo-V gas shielded flux-cored wire, and subjected to dynamic impact abrasive wear tests under different impact energy. Microstructures and wear scar characteristics of deposited metal were characterized by scanning electron microscopy with energy disperse spectroscopy, weight loss test, and laser scanning confocal microscopy to investigate the abrasive wear behavior of deposited metal under different impact energy. The results show that the microstructure of deposited metal is mainly composed of austenite, lamellar eutectic structure, and spherical VC hard phases. The wear loss of deposited metal, the roughness of the wear scar, and the depth of the wear scar gradually decrease with the increase of impact energy. The wear mechanism are the micro-cutting of the austenite matrix by the abrasive grains and plastic deformation. As the impact energy increases, the deposited metal undergoes work hardening, and a deformed martensite structure appears on the subsurface of the wear scar. Furthermore, the VC hard phase interacts with the lamellar eutectic structure to increase the hardness of the deposited metal, thereby improving the wear resistance of the matrix and

enhancing the impact resistance.

Key words: Fe-C-Mo-V hardfacing alloys; impact energy; abrasive wear; deformation martensite

X-ray stress measurement process of aluminum alloy by analysis of the full width at half maxima WANG Xiaopeng, LI Xiaoyan, XU Zhou, WU Qi (Beijing University of Technology, Beijing 100124, China). pp 86-90

Abstract: In this paper, X-ray method is used to test the residual stress of 6061-T6 aluminum alloy welded joints. In order to explore a reasonable stress measurement process, X-ray stress test is performed on the pre-stressed equal-strength beam. The diameter of the aperture and the oscillation angle are successively increased during the test. The full width at half maximum of the diffraction profile is used to characterize the microscopic strain of the diffracted grain group. The change in the uniformity of the microscopic strain of the diffracted grain group is analyzed when the aperture diameter and oscillation angle increase, as wll as performing orientation imaging analysis to compare the grain selection between two stress test scheme in different intervals of preferred orientation of the grains. The results show that the stress test accuracy is related to the strength of the preferred orientation of the grains. In the spatial range where the preferred orientation of the grains is strong, when oscillation angle greater than 1° is used, the adjacent sub-crystals near the small-angle grain boundary can participate in the diffraction, so that the microscopic strain of the diffracted crystal grain group tends to be uniform, so the X-ray stress measurement accuracy is higher, and when the aperture is added in the range of d = 2 ~ 4 mm, the increase of diameter d can increase the number of diffracted grains, but has little effect on the microscopic strain uniformity of the diffracted grain group and the accuracy of stress testing.

Key words: stress measurement; X-ray; microstrain; measurement process

Process optimization of projection welding of nut based on regression analysis XING Xiaofang[1], BEN Qiang[2], ZHOU Yong[1], LU Hao[1], HAN Pei[1] (1. Xi'an Shiyou University, Xi'an, 710065, China; 2. Chinese People's Liberation Army No. 5720 Factory, Wuhu, 241000, China). pp 91-96

Abstract: Single factor experimental design was used for M6 welded square nuts and SAPH370 pickled hot-rolled steel plates in order to optimize the nut welded joint quality. The electrode force, welding current and welding time were picked out as the process parameters and the Pull-out load were weighted into a welding quality index. The mathematical model between the welding quality index and process parameters was obtained by regression analysis. The research results show that the welding current has the greatest effect on the Pull-out load, and the welding time and electrode pressure have a small effect on the Pull-out load. When the electrode pressure is small, the welding time has a large effect on the Pull-out load. When the electrode pressure is large, the welding current has a large effect on the Pull-out load. The interaction effect between electrode pressure and welding current is the largest, the interaction effect between welding current and welding time and the interaction effect between electrode pressure and welding time are smaller.

Key words: projection welding of nut; SAPH370; the pull-out load; regression model; welding quality